DETC2024-143495

MODELING AND CONTROL CO-DESIGN OF A FLOATING OFFSHORE VERTICAL-AXIS WIND TURBINE SYSTEM

Yong Hoon Lee[1,*], Saeid Bayat[2], James T. Allison[2], Md Sanower Hossain[3], D. Todd Griffith[3]

[1]The University of Memphis, Memphis, TN
[2]University of Illinois at Urbana-Champaign, Urbana, IL
[3]University of Texas at Dallas, Richardson, TX

ABSTRACT

This study investigates the modeling and design of a floating vertical-axis wind turbine (FloatVAWT) system with multidisciplinary design optimization (MDO) and control co-design (CCD) approaches. By integrating various associated disciplinary models, the study aims to holistically optimize the physical and control designs of the FloatVAWT system. Through the identification of impactful design elements and capitalizing on synergistic interactions, the study aims to provide insights to subsystem designers and aid their detailed decisions. The model developed for this CCD framework utilizes automated geometric manipulation and mesh generation to explore various FloatVAWT configurations during the early design stages. Surrogate models facilitate efficient design studies within limited computing resources by exchanging model information between disciplinary models and subsystems without running exhaustive simulations during the optimization loop. The model incorporates an aero-hydro-servo dynamic representation of the FloatVAWT system, considering physical and control constraints. Additionally, the study investigates the potential benefits of varying the average rotational speed of the vertical-axis wind turbine (VAWT) rotor to enhance energy production and minimize adverse platform motions, thus reducing the levelized cost of energy (LCOE). System-level design solutions are analyzed to identify design trade-offs and propose mitigation strategies for potential mechanical failures of the rotor. In conclusion, this study provides modeling strategies for the FloatVAWT system and analyzes the system design solutions through MDO and CCD approaches. The outcomes of the study offer insights into system-optimal solutions for subsystem-level decisions considering multidisciplinary couplings.

Keywords: floating offshore wind turbine (FOWT), vertical-axis wind turbine (VAWT), control co-design (CCD), multidisciplinary design optimization (MDO), intracycle RPM control

*Corresponding author: yhlee@memphis.edu

1. INTRODUCTION

The untapped potential for offshore wind energy in the deep-water regions within the exclusive economic zone (EEZ) of the United States is substantial [1]. Tapping this potential demands the use of floating platforms, as fixed foundations are not viable with the water depths in these locations. The main obstacle to the deployment of floating offshore wind turbines (FOWTs) is the cost of a floating platform, which typically takes the most considerable portion of the total levelized cost for FOWT designs [2]. Therefore, it is crucial to focus on developing cost-effective FOWTs, such as the floating vertical-axis wind turbine (FloatVAWT) concept [3], to address and overcome these challenges.

In recent years, there has been significant development in various general simulation and design codes for FOWTs, such as OpenFAST [4], QBlade [5], and WEIS [6]. In addition, aero-hydro-servo models tailored for specific FOWT configurations have been developed and applied in various design studies [7–11]. However, only a limited number of codes have the capability for aero-hydro-servo simulation and optimization with vertical-axis wind turbine (VAWT) configurations [12, 13].

The inherent limited control authority of typical VAWT rotors has resulted in relatively few control studies in the literature [14]. These studies often introduce additional control degrees of freedom (DOFs), such as individual pitch control [15] or supplementary flapping wings behind the main rotor blades [16], which may not be universally applicable to all VAWT designs. Moreover, prior research on the rotational speed of VAWT rotors has focused and optimized considering structural damping ratio [17] or solidity impact to rated rotational speed [18]. However, these studies do not account for continuous variations in rotational speed under transient wind conditions to maximize energy production.

Until recently, VAWTs have gained little attention as candidates for commercial-scale land-based wind turbines due to inherent disadvantages such as relatively lower efficiency, cyclic torque
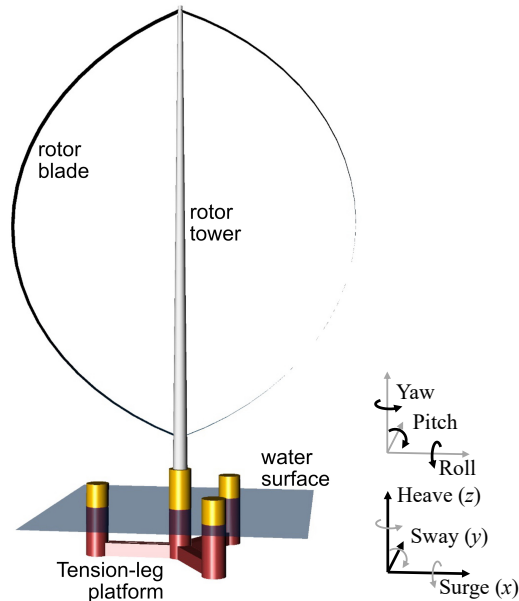
FIGURE 1: General layout of the floating vertical-axis wind turbine.

ripple, and dynamic stall characteristics [19, 20]. However, when integrated into FOWT systems, VAWTs offer a notable advantage due to their lower vertical center of gravity (COG) [12]. This advantage makes VAWT particularly suitable for FOWT applications, and overall cost efficiency can be enhanced by minimizing the expenses associated with the floating platform.

In this paper, a tension-leg platform (TLP) design with three outer columns and one center column connected by three underwater pontoons is considered. The size and mass distribution of this configuration are optimized, along with control of the VAWT generator torque. With this framework, we solve the system-level control co-design (CCD) problem to achieve minimized levelized cost of energy (LCOE) and inform system-optimal solutions for subsystem-level decisions while maintaining hydrostatic stability for wet towing (without mooring system) and in-place hydrodynamic stability (with mooring system), considering multidisciplinary system couplings using multidisciplinary design optimization (MDO) approach [21]. This design optimization framework accommodates various system configurations through automated geometric manipulation and mesh generation of the TLP configuration and utilizes surrogate models in exchanging model information between subsystems to efficiently support design studies within limited computing resources.

Additionally, employing variable rotational speed within a single revolution of the VAWT rotor, known as intracycle RPM control, offers further enhancements in VAWT efficiency [22]. This previous research laid the groundwork for this study. Moreover, by considering intracycle RPM with continuous variations in average rotational speed under transient wind conditions, further efficiency improvement could be achieved. Our research demonstrates that optimizing both the intracycle RPM and the average rotational speed varying across a range of wind speeds can concurrently improve overall annual energy production (AEP) while reducing the potential mechanical failure of the rotor system through optimization.

2. METHODS

2.1 Structure of the Design Optimization Framework

The design framework for the FloatVAWT system, as an outcome of the FloatVAWT project [3] given in Fig. 1, is constructed to optimize the variables associated with both the floating platform plant and the rotor generator control. The optimization problem aims to achieve the lowest possible LCOE while satisfying all physical and control constraints. Figure 2 provides an extended design structure matrix (XDSM) [23] of the FloatVAWT system design problem structure.

The system optimizer drives the entire design problem by providing plant and control design candidates (d_{plant} and α_{ctrl}) to all disciplinary models. In this study, we used COBYLA algorithm as the system optimizer [24]. The objective function, LCOE, is derived by dividing the estimated overall cost by the calculated AEP. Cost models for FOWT systems are typically complex, enompassing both capital and operating expenses, while also accounting for market prices and financial costs. However, in this study, the cost model is simplified by using the platform mass as a proxy to the cost. The AEP is calculated by the turbine energy production subsystem, based on steady state power production from the optimal rotor control solution, incorporating a probabilistic wind speed distribution. The optimal rotor control solutions provided to the system design problem is based on the intracycle RPM control surrogate model, trained separately to obtain the average power and the vector of thrust and lateral forces (F_{avg}) for each wind speed among wind speed bins between cut-in and cut-out wind speeds. The training process of this surrogate model, presented in Fig. 3, uses the solutions for the intracycle RPM control problems.

The TLP design models are solved using a multidisciplinary analysis (MDA) solver. Particularly, achieving hydrostatic stability involves an iterative solution process where intermediate solutions do not provide insights for rotor and control disciplines. Consequently, the platform design segment is isolated using MDA structure, to solely deliver feasible platform design solutions to the system optimizer. The cost associated with the platform is assumed to vary linearly with the system mass, using a proprietary TLP design as a reference point. The hydrodynamic effect of the floating platform system provides the time-averaged platform pitch angle, which is used to calculate the effective wind speed perpendicular to the rotational axis of the VAWT rotor. This coupling implies that both floating platform plant and rotor control designs impact the calculation of the LCOE objective function.

The subsystem modules depicted in Figs. 2 and 3 utilize turbine, platform, and metocean data as fixed inputs to define the specifications of the FloatVAWT system configuration. These predefined design specifications are outlined in YAML, a standardized data serialization format. This approach enhances the flexibility of the optimization framework, enabling it to accommodate diverse turbine scales, design configurations, and metocean conditions. Within exhaustive list of parameters provided by these YAML files, a subset of TLP plant parameters and control parameters can be chosen for design optimization.

The TLP design consists of three parts: geometry, hydrostatics, and hydrodynamics. The geometry model computes mass, vertical and radial centers of gravity, and mass moment of inertia
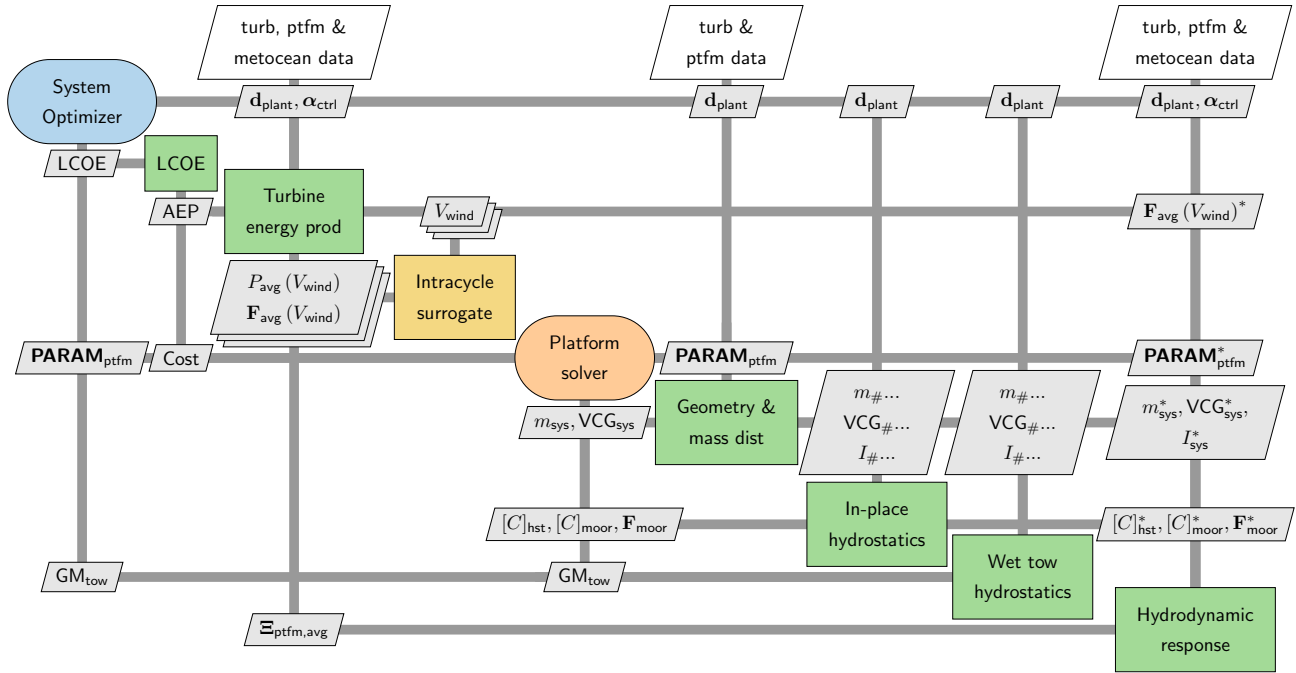
FIGURE 2: Extended design structure matrix (XDSM) for system design problem structure of the floating vertical-axis wind turbine (Float-VAWT) optimization framework. The XDSM presented here is simplified representation and may not encompass all variables or connections.
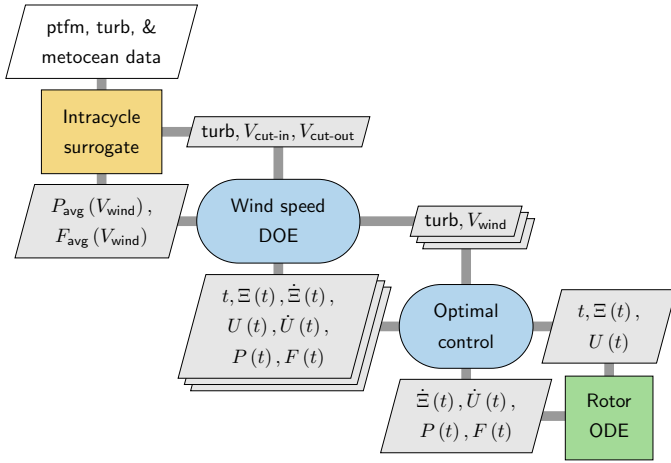

FIGURE 3: XDSM for training the surrogate model for the intracycle RPM control component of the FloatVAWT optimization framework.

(MOI) in roll, pitch, and yaw directions for each system component. This model uses platform design variables and fixed parameters, including dimensions, ballast design, mooring design, and platform draught configurations, along with turbine specification parameters. Hydrostatic simulations are performed for both in-place and wet tow conditions and provide hydrostatic stiffness matrix, metacentric height, and mooring line stiffness matrix. System dynamic simulation is performed using the aero-servo-hydro simulation model for the reference platform and turbine design [12]. Then, the time-averaged platform pitch motions for varied platform designs are estimated relatively using the variance of the floating platform hydrodynamic added mass matrix, assuming that the variances of hydrodynamic forces have lin-

early proportional correlations with the added mass variance for simplicity in computation.

2.2 Tension-Leg Platform Geometry and Mesh

The system cost model for FOWT primarily depends on the overall platform mass. Additionally, the hydrostatic and hydrodynamic coefficients are heavily influenced by the submerged platform shape, freeboard shape, and the distribution of mass within the system. Therefore, accurate representation of the system geometry and mass distribution is crucial for conducting CCD studies. Geometry and boundary element panel meshes of the TLP design used in this study are illustrated in Fig. 4. The structural components primarily consist of a cylindrical center column, cylindrical outer columns, and pontoons with rectangular cross-sections connecting the outer columns to the center column positioned at the bottom (keel) of the TLP structure. For computing hydrostatics and hydrodynamics of the system, meshes for the submerged portion of the platform for in-place and wet tow conditions need to be created. However, the freeboard (above the water line) portion of the platform must also be considered when computing mass, vertical and radial centers of gravity, and MOI for three rotational DOFs. Detailed methods for calculating these quantities are given in Appx. A.

2.3 Hydrostatics and Hydrodynamics

The hydrostatic stiffness matrix for a floating body is computed by integrating the following equation over the immersed surface elements [25]:

$$C_{ij} = \rho g \iint_S (\hat{n} \cdot \text{DOF}_j)(w_i + z\nabla \cdot \text{DOF}_i)\, dS \qquad (1)$$

where $\text{DOF}_i = u_i\hat{n}_x + v_i\hat{n}_y + w_i\hat{n}_z$ is DOF vector, u, v, w are DOF displacements in x, y, z directions, and $\hat{n}$ is surface normal unit
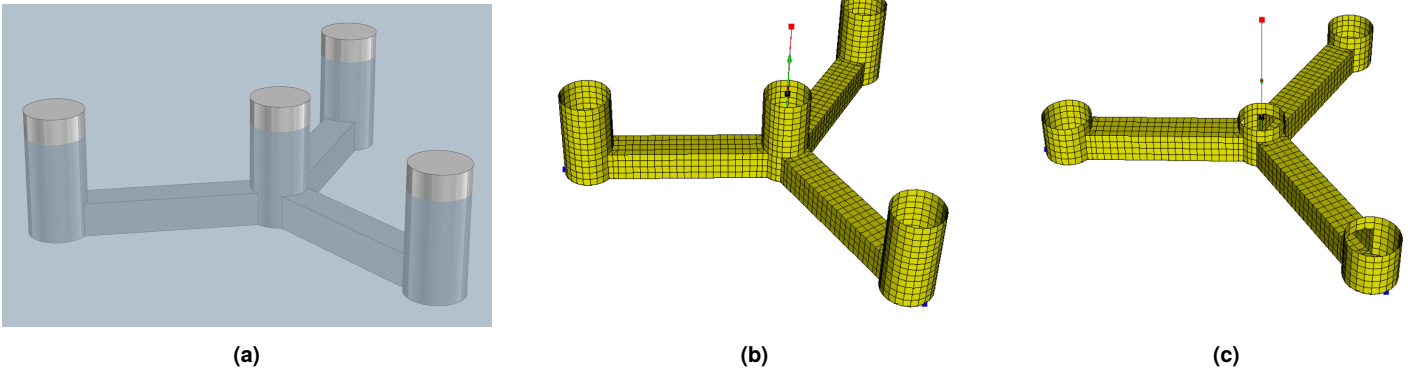
FIGURE 4: Geometry and boundary element (panel) meshes of the TLP designed for the FloatVAWT system. (a) TLP geometry shown with in-place draught. **(b)** Panel mesh representing the in-place condition of the submerged portion of the TLP. **(c)** Panel mesh representing the submerged portion of the TLP in wet tow condition.

vector. The hydrostatic stiffness for in-place condition, given in Fig. 4(b), is directly used as a part of system stiffness to provide hydrostatic recovering force in the system dynamic equation.

The main purpose of computing hydrostatic stiffness matrix for wet tow condition, given in Fig. 4(c), is to ascertain if the FloatVAWT structure can be safely towed to the installation site without support of mooring line tension. As the system undergoes optimization, hydrostatic stability is assessed in terms of the metacentric height (GM), provided as a physical constraint in the system-level optimization formulation. GM is calculated as:

$$\text{GM} = \min\left(\text{GM}_x,\ \text{GM}_y\right) \tag{2a}$$

$$\text{GM}_x = -\frac{1}{V_{\text{sm}}}\int_S x^2\, dS - \left(\text{COG}_{\text{sys}} - \text{COB}_{\text{sys}}\right) \tag{2b}$$

$$\text{GM}_x = -\frac{1}{V_{\text{sm}}}\int_S y^2\, dS - \left(\text{COG}_{\text{sys}} - \text{COB}_{\text{sys}}\right), \tag{2c}$$

where COB_{sys} is center of buoyancy of the system.

The hydrodynamic response of the baseline system design is calculated using the model developed in Ref. [12] and serves as a reference point for determining the average platform pitching motion. The hydrodynamic responses of the perturbed designs are estimated through a combination of factors: (1) linear variation relative to the aerodynamic thrust and lateral forces and (2) a simplified estimation of amplitude difference using a mass-spring system with a combined system stiffness matrix, given as:

$$\Xi_{\text{avg,pitch}} = \Xi_{\text{avg,pitch,}\atop\text{baseline}} \cdot \frac{F_{\text{thrust}}}{K_{\text{sys,pitch}}} \cdot \frac{K_{\text{sys,pitch,}\atop\text{baseline}}}{F_{\text{thrust,}\atop\text{baseline}}}, \tag{3a}$$

$$\Xi_{\text{avg,roll}} = \Xi_{\text{avg,roll,}\atop\text{baseline}} \cdot \frac{F_{\text{lateral}}}{K_{\text{sys,roll}}} \cdot \frac{K_{\text{sys,roll,}\atop\text{baseline}}}{F_{\text{lateral,}\atop\text{baseline}}}, \tag{3b}$$

where Ξ_{avg} is the average amplitude of the system motion, F_{thrust} and F_{lateral} are aerodynamic thrust and lateral forces applied to the turbine, and K_{sys} is the combined system stiffness. This assumption disregards hydrodynamic damping and only considers hydrostatic stiffness and mooring line stiffness. Mooring line

stiffness, K_{moor} (6×6 matrix) is calculated as [26]:

$$K_{11} = K_{22} = \frac{n_{\text{leg}}F_{\text{pre}}}{L_{\text{leg}}} \tag{4a}$$

$$K_{33} = \frac{n_{\text{leg}}K_{\text{leg}}}{L_{\text{leg}}} \tag{4b}$$

$$K_{44} = K_{55} = n_{\text{leg}}\left(\frac{F_{\text{pre}}H_{\text{fair}}^2}{L_{\text{leg}}} + \frac{K_{\text{leg}}R_{\text{fair}}^2}{2L_{\text{leg}}} + F_{\text{pre}}H_{\text{fair}}\right) \tag{4c}$$

$$K_{66} = \frac{n_{\text{leg}}F_{\text{pre}}R_{\text{fair}}^2}{L_{\text{leg}}} \tag{4d}$$

$$K_{24} = K_{42} = \frac{n_{\text{leg}}F_{\text{pre}}H_{\text{fair}}}{L_{\text{leg}}} = -K_{15} = -K_{51}, \tag{4e}$$

where n_{leg} is the number of tension legs, F_{pre} is the pretension force applied to each tension leg, L_{leg} is the length of the tension legs, K_{leg} is the lengthwise line stiffness of the tension legs, H_{fair} is the depth of the fairlead location under the platform DOF center, and R_{fair} is the offset radial distance of the fairlead from the center axis of the platform DOF center. Here, fairlead and tension leg dimensions are dependent on the TLP design by the following relationships, assuming that the system DOF center is located at the water surface:

$$L_{\text{leg}} = H_{\text{water}} - H_{\text{dr}} \tag{5a}$$

$$H_{\text{fair}} = H_{\text{dr}} \tag{5b}$$

$$R_{\text{fair}} = L_{\text{pont}} + D_{\text{oc}} + \frac{D_{\text{cc}}}{2} \tag{5c}$$

where H_{water} is the water depth. As we did not change the rotor (tower and blade) design, the pressure center of the rotor remains the same and canceled out from this equation.

As the purpose of the system-level design problem is to provide design guidelines for detailed subsystem design decisions, detailed time-domain system dynamic simulations are not conducted during system-level optimization. The system dynamics of the candidate design is roughly estimated with the variances in hydrodynamic coefficients of the platform, system mass distribution, and aerodynamic loadings. Consequently, if the design solution is intended for later-stage practical applications, a thorough safety assessment must be additionally conducted, including

the system dynamic simulations for international electrotechnical commission (IEC) design load cases (DLCs) for FOWT systems [27].

2.4 Intracycle RPM Control

The VAWT rotor system considered in this study has rotor rotational DOF about the axis perpendicular to the wind stream and also perpendicular to the water surface, as shown in the top part of Fig. 1. The rotational motion is controlled by regulating generator torque. The aerodynamic characteristics of the VAWT rotor are obtained by using the CACTUS code [28] for varied wind speeds between cut-in and cut-out wind speeds.

Control over the rotational motion is achieved by regulating the generator torque. The aerodynamic properties of the VAWT rotor are analyzed using the CACTUS code over one revolution and across a range of wind speeds from cut-in to cut-out thresholds, i.e., 5 to 25 m/s. The aerodynamic properties obtained are in functions of the azimuth angle of the rotor (θ). Surrogate models for these aerodynamic properties are constructed using two-dimensional cubic splines with full factorial sample points, similarly to Ref. [22]. The use of this surrogate model is to expedite the optimization process, rather than relying on direct access to the CACTUS code by the optimizer. The list of aerodynamic properties used for solving the intracycle RPM control problem includes azimuth rate or rotational speed (ω) of the rotor, aerodynamic torque (T), aerodynamic thrust (F_{thrust}) and lateral (F_{lateral}) forces, and power (P). The VAWT rotor system optimal control problem formulation for a combination of given wind speed, α, and β values is given as:

$$\underset{t_f, \, \boldsymbol{\xi}, \, u}{\text{minimize}} \quad -P_{\text{obj}} = -\int_{t_0}^{t_f} \frac{\left(\xi_3\left(t\right)\xi_2\left(t\right) - c_1\xi_3^2\left(t\right) - c_2 u^2\left(t\right)\right)}{t_f - t_0}\,dt$$

$$\text{subject to} \quad \dot{\boldsymbol{\xi}}\left(t\right) = \left[\xi_2\left(t\right), \, \frac{T\left(\xi_2\left(t\right), \xi_1\left(t\right)\right) - \xi_3\left(t\right)}{I_{zz,\text{rotor}}}, \, u\left(t\right)\right]$$

$$\xi_1\left(t_0\right) = 0$$

$$\xi_1\left(t_f\right) - 2\pi = 0$$

$$\xi_2\left(t_f\right) - \xi_2\left(t_0\right) = 0$$

$$\xi_3\left(t_f\right) - \xi_3\left(t_0\right) = 0$$

$$F_{\text{lateral}}\left(\xi_2\left(t\right), \xi_1\left(t\right)\right) - \alpha F_{\text{lateral,max, baseline}} \le 0$$

$$F_{\text{thrust}}\left(\xi_2\left(t\right), \xi_1\left(t\right)\right) - \beta F_{\text{thrust,max, baseline}} \le 0$$

$$\text{where} \quad \boldsymbol{\xi} = \left[\xi_1\left(t\right), \, \xi_2\left(t\right), \, \xi_3\left(t\right)\right] = \left[\theta\left(t\right), \, \omega\left(t\right), \, T_{\text{gen}}\left(t\right)\right]$$

$$u = \dot{T}_{\text{gen}}\left(t\right). \tag{6}$$

Here, t_0 and t_f are starting and ending time for a single rotor revolution, $\boldsymbol{\xi}$ is the state vector containing rotor azimuth angle, rotational speed, and generator torque (T_{gen}), u is the control signal, representing the time rate of change of the generator torque ($\dot{T}_{\text{gen}}$). As we optimize the average rotor rotational speed, terminal time, t_f, is included in the set of design variables, and maximizing power as our objective function (P_{obj}) instead of maximizing the energy production used in Ref. [22]. This optimal control problem corresponds to the "Optimal control" and "Rotor ODE" blocks of the XDSM provided in Fig. 3. It is discretized by the Radau pseudospectral method using Dymos optimal control code [29, 30].

2.5 System Design Optimization Formulation

The system-level design problem is formulated by integrating the subsystem components discussed in the preceding sections and given as:

$$\underset{\mathbf{d}_{\text{ptfm}}, \, \boldsymbol{\alpha}}{\text{minimize}} \quad \text{LCOE} = \frac{\text{Cost}_{\text{sys}}}{\text{AEP}_{\text{sys}}}$$

$$\text{subject to} \quad \text{Cost}_{\text{sys}} - \text{fac}_{\text{cost}} m_{\text{sys}} = 0$$

$$\text{AEP}_{\text{sys}} - \text{AEP}_{\text{aero}} \cos\left(\Xi_{\text{avg,pitch}}\right) = 0$$

$$\rho_{\text{water}} V_{\text{disp}} - \left(m_{\text{sys}} + \frac{F_{\text{pre}}}{g}\right) = 0$$

$$\rho_{\text{water}} V_{\text{disp,tow}} - \left(m_{\text{sys}} - m_{\text{bal}}\right) = 0$$

$$\text{GM}_{\text{min}} - \text{GM} \le 0$$

$$L_{\text{yard}} - L_{\text{yard,max}} \le 0$$

$$\text{where} \quad \text{fac}_{\text{cost}} = \frac{\text{Cost}_{\text{baseline}}}{m_{\text{sys, baseline}}}$$

$$\text{AEP}_{\text{aero}} = t_{\text{yr}} \int_{V_{\text{wind}}} \text{PDF}\left(V_{\text{wind}}\right) P\left(V_{\text{wind}}, \alpha_{V_{\text{wind}}}\right)$$

$$L_{\text{yard}} = \left(1 + \cos\frac{\pi}{3}\right)\left(D_{\text{oc}} + L_{\text{pont}} + \frac{D_{\text{cc}}}{2}\right)$$

$$\mathbf{d}_{\text{ptfm}} = \left[D_{\text{oc}}, H_{\text{dr}}, L_{\text{pont}}, m_{\text{bal}}, H_{\text{dr,tow}}, F_{\text{pre}}\right]$$

$$\boldsymbol{\alpha} = \left[\alpha_{V_{\text{cut-in}}}, \cdots, \alpha_{V_{\text{cut-out}}}\right] \tag{7}$$

Here, V_{disp} and $V_{\text{disp,tow}}$ are the water volume displaced by the submerged structure at in-place and wet tow conditions, respectively. These quantities are calculated by the submerged structure panel mesh given in Fig. 4(4b), which should match the value of the analytical submerged volume, V_{sm}. The minimum metacentric height, GM_{min}, is established at 2.0 m for this study. This particular value needs to be adjusted depending on the overall scale of the turbine. $L_{\text{yard,max}}$ represents the length dimension of the shipyard wet dock where manufacturing will take place. fac_{cost} is the cost factor based on the cost analysis data for the baseline design, t_{yr} is hours in one year, which is 8,760 hours, PDF is the probability density function for wind speed, calculated using the Weibull distribution, and shown in Fig. 5(a), $\mathbf{d}_{\text{ptfm}}$ is the plant design variable vector for the TLP design parameters, and $\boldsymbol{\alpha}$ is the control design variable vector for defining the peak load factors (α and β) for each wind speed bins.

3. RESULTS AND DISCUSSIONS

This section presents the results of both the intracycle RPM control optimization and the system-level CCD optimization studies. The intracycle RPM control problems are solved using the pseudospectral optimal control method, with aerodynamic properties modeled through cubic spline surrogate models, as described in Sect. 2.4. The result from the first part (Sect. 3.1, intracycle RPM control) include time-dependent trajectories of power outputs and aerodynamic forces across varied wind speed bins. This dataset is then utilized to construct a Kriging surrogate model, which forms the control model for the second part of the study (Sect. 3.2, system-level CCD) focusing on system-level CCD optimization.
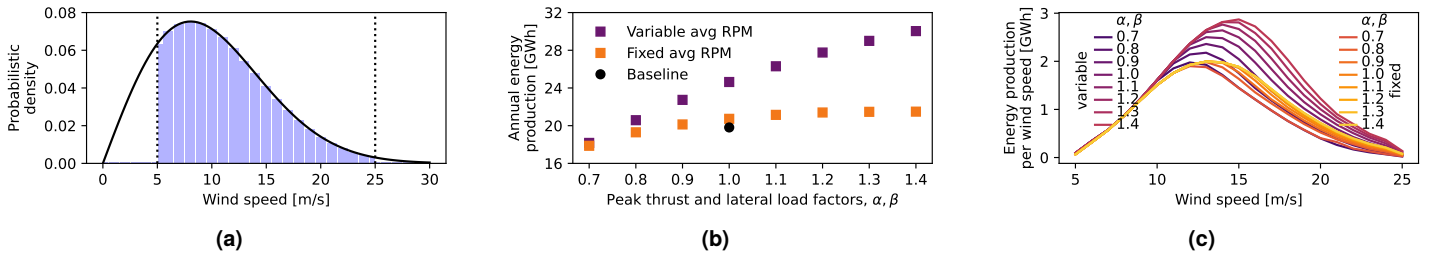
FIGURE 5: Wind speed probabilistic distribution and optimal energy production results with respect to the wind probability. Fixed and variable average rotor velocity cases are compared. (a) Wind speed probability density function (PDF) employing Weibull distribution. Vertical dotted lines represent cut-in and cut-out speeds. (b) Annual energy production (AEP) for varied peak load factor values. (c) Energy production per wind speed for varied peak load factor values. Variable refers to the variable average RPM cases and fixed refers to the fixed average RPM cases.
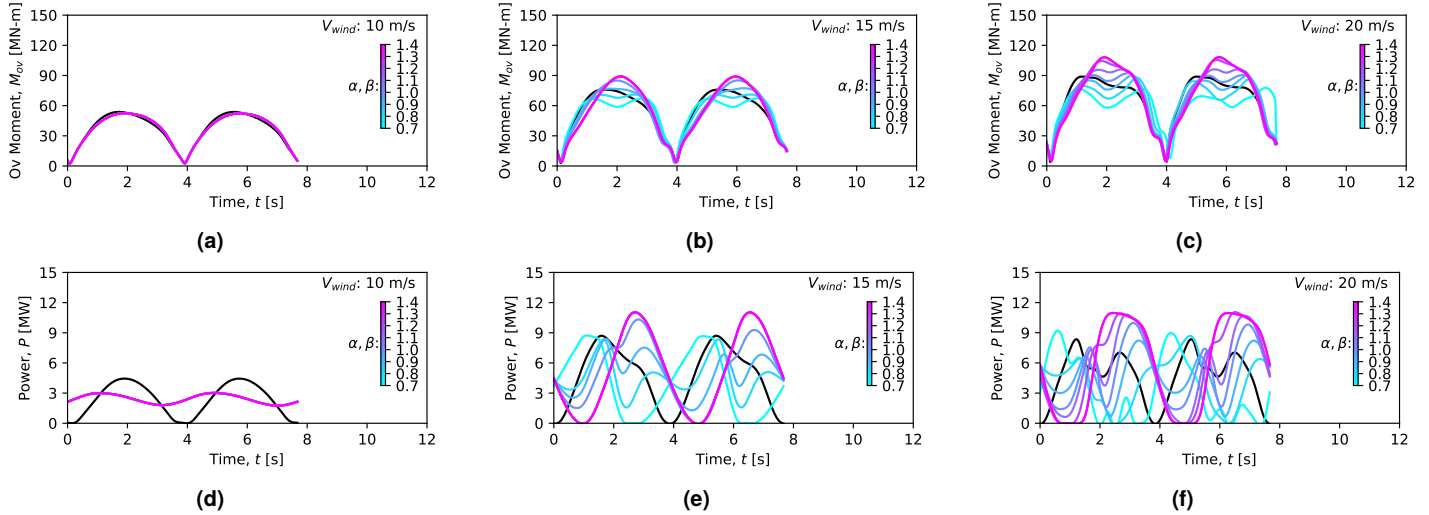

FIGURE 6: Intracycle RPM control result for fixed average rotor velocity case. Lines with color gradation are optimal control results, and black lines are baseline design results. (a)–(c) Aerodynamic overturning moment for wind speeds 10, 15, and 20 m/s. (d)–(f) Generator power for wind speeds 10, 15, and 20 m/s.

3.1 Fixed and Variable Average Rotor Velocity

The intracycle RPM control study is performed for varied constraints on peak thrust and lateral loads (by varying load factors, α and β), following Ref. [22], and for varied wind speeds between cut-in and cut-out thresholds, as shown in Fig. 5(a). Two distinctive cases are studied: (1) one with fixed average rotor velocities and (2) another with variable average rotor velocities. Figure 5(b) illustrates the AEP results for these cases across varying peak load values. In this figure, darker (purple) square markers denote AEP results with variable average rotor rotational speed, while lighter (orange) square markers represent those with fixed average rotor rotational speed. Figure 5(c) displays the distribution of energy production contributions across varied wind speeds for each peak load case. Results shown here account for the wind probabilistic density variations, shown in Fig. 5(a). For both fixed and variable average rotor rotational speed cases, energy extraction is improved for higher wind speeds when the peak load constraint is relaxed by increasing α and β values. Notably, the variable rotor rotational speed case gives higher power output, as it allows the rotational speed as another design freedom for optimal energy production. Thus, this case is further used for the overall system-level design problem, presented in Sect. 3.2.

Figures 6 and 7 shows overturning moment and power trajectories at relatively higher wind speeds (10, 15, and 20 m/s), while Fig. 8 shows power trajectories at lower wind speeds (5, 6, and 7 m/s). Based on the probabilistic density given in Fig. 5(a), lower wind speeds dominate over the lifetime of the wind turbine, influencing overall accumulation of number of rotor revolutions. However, higher wind speed creates higher overturning moment, making constraints on peak thrust and lateral loads active. Thus, higher wind speeds are main driver limiting the overall design of the floating platform and control parameters.

Figure 6 presents the representative optimal control results solved for the fixed average rotor rotational speed scenario. In (a)–(c), aerodynamic overturning moment trajectories are depicted for wind speeds of 10, 15, and 20 m/s. Similarly, (d)–(f) illustrates generator power trajectories corresponding to the same wind speeds. In this scenario, the rotor rotational speed is regulated within a single revolution to maximize power extraction. However, the time required for a single revolution remains constrained to match that of the baseline case, thereby ensuring a fixed average rotational speed.

Figure 7 presents the representative optimal control results solved for the variable average rotor rotational speed scenario.
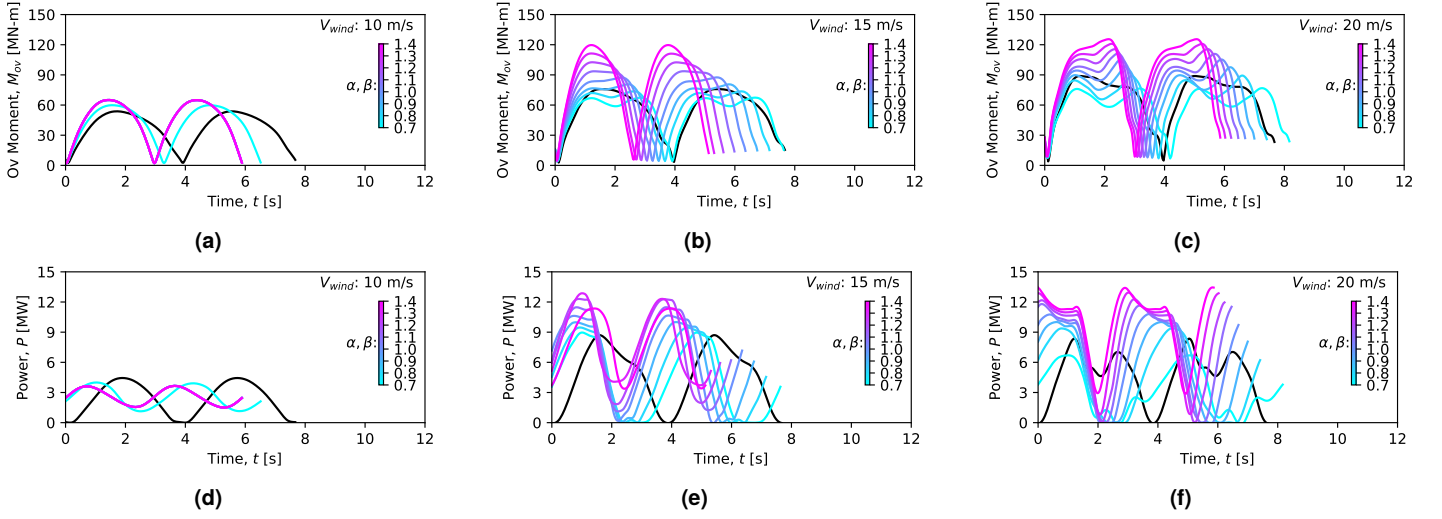
FIGURE 7: Intracycle RPM control result for variable average rotor velocity case. Lines with color gradation are optimal control results, and black lines are baseline design results. (a)–(c) Aerodynamic overturning moment for wind speeds 10, 15, and 20 m/s. (d)–(f) Generator power for wind speeds 10, 15, and 20 m/s.
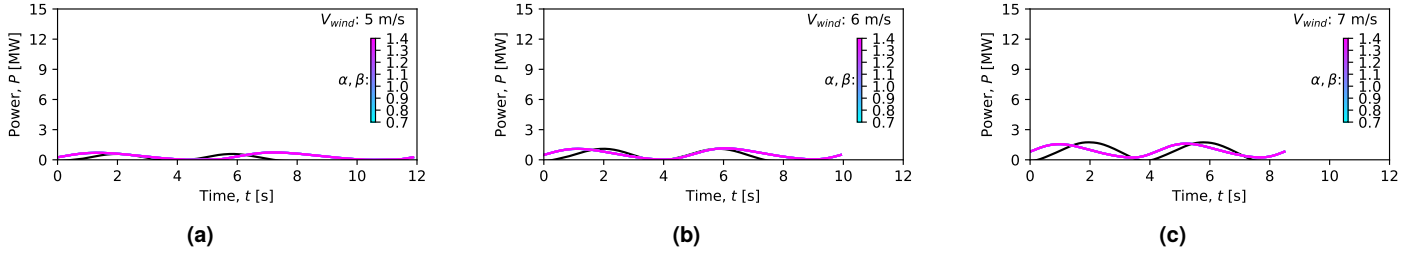

FIGURE 8: Lower wind speed generator power from intracycle RPM control result for variable average rotor velocity case. Lines with color gradation are optimal control results, and black lines are baseline design results. Since the peak load constraints are not active for lower wind speed cases, varying α and β values do not change the result. (a)–(c) corresponds to wind speeds 5, 6, and 7 m/s, respectively.

In (a)–(c), aerodynamic overturning moment trajectories are depicted for wind speeds of 10, 15, and 20 m/s. Similarly, (d)–(f) illustrates generator power trajectories corresponding to the same wind speeds. Notably, for all plots in (a)–(f), the time required for a single revolution varies as the rotor rotational speed is regulated to maximize power extraction. Allowing higher aerodynamic loads by relaxing peak load constraint (α and β) accelerates the overall rotor rotational speed to extract larger energy, while tighter peak load constraint keeps the average rotor rotational speed closer or even slower than that of the baseline case.

The results depicted in Figs. 6 and 7 selectively showcase the optimal control results of wind speeds 10, 15, and 20 m/s. These results highlight significant variations across different peak load constraint values. However, considering the probabilistic wind speed distribution presented in Fig. 5(a), it becomes evident that the FloatVAWT system is expected to experience wind speeds ranging from 5 to 10 m/s for a significant portion of its operational lifetime. Figure 8 presents the power trajectories of the lower wind speed optimal control results for the variable average rotor rotational speed scenario. Energy production is significantly lower than in higher wind speed cases, and the optimal average rotor rotational velocities are found to be significantly slower. These results emphasize that it is not always optimal to run at faster rotational speed, and for certain low wind speed con-

TABLE 1: System design solutions

Variable	Unit	Fixed Avg ω	Variable Avg ω
D_{oc}	m	6.7338	6.7635
H_{dr}	m	14.500	14.505
L_{pont}	m	23.112	22.976
m_{bal}	tonne	86.998	87.000
$H_{dr,tow}$	m	5.9728	5.9835
F_{pre}	tonne	1186.2	1193.5
$\bar{\alpha} \leq 1.2$	-	1.1657	1.1076
L_{yard}	m	49.077	48.926
Cost	M\$	2.6180	2.6187
AEP	GWh	21.756	28.031
LCOE	\$/kWh	0.12033	0.09342

ditions, the lower rotational velocities may produce more energy. Furthermore, the lower average rotational velocities at lower wind speeds contribute to keeping the accumulated number of annual rotor revolution values similar to the baseline case, keeping less chance for mechanical failures.

3.2 System-Level Control Co-Design Solution

System-level CCD solutions are summarized in Tab. 1. As anticipated from the intracycle RPM control solutions detailed in Sect. 3.1, the CCD solution achieved for the variable average rotor rotational speed scenario yields an improved LCOE primarily due to a significantly increased AEP value compared to the CCD solution obtained for the fixed average rotor rotational speed scenario. The design solutions given in Tab. 1 show that the change in control schemes dominates the performance change, while differences in plant design variables remain very close to each other. Two factors described in the subsequent paragraphs are responsible for this result.

First, given the inherent stability of TLPs, attributed to their substantial pretension force limiting platform motion, the coupling between TLP plant design variables and rotor control variables is minimal. Nonetheless, optimal solutions reveal that different control strategies lead to slightly different optimal plant configurations. The significant improvement in LCOE for variable rotor rotational speed is primarily due to the control design. Thus, based on our CCD study, the optimal FloatVAWT design presented here with the TLP foundation is predominantly driven by the optimal control subsystem.

Furthermore, the optimal control constraints on thrust and side to side forces set the maximum limits of aerodynamic loading that influences the floating platform motion. These constraints are essential for rotor designers to use as reference in their detailed design process. However, more intricate interactions between control and plant designs might emerge if these constraints are replaced by constraints based on detailed structural models for rotor directly implemented in the optimal control problems. Specifically, if accurate models for predicting rotor blade stress and fatigue damage were available, then rather than simply constraining thrust and side to side forces, varying profiles of aerodynamic forces from different control strategies could influence variations in plant design variables. This potential impact demand further investigation in future research.

4. CONCLUSION

In this study, we have presented MDO modeling and CCD optimization of a TLP-based FloatVAWT system. The model integrated an aero-hydro-servo dynamic representation of the FOWT system with FloatVAWT concept [3], considering various physical and control constraints. By integrating various disciplinary domain models, we aimed to achieve an optimal system design by capitalizing on synergistic interactions between different physical and control design elements. We explored the possibilities of variable average rotational speed of the VAWT rotor with the intracycle RPM control for enhanced energy production and minimized platform motions, ultimately reducing the LCOE.

The system design solutions were analyzed for minimized LCOE, design trade-off considerations, and potential mitigation strategies for potential mechanical failure of the rotor. The TLPs offer a highly stable foundation for the FOWT systems, minimizing the couplings between physical and control systems. Optimal solutions revealed that optimal control strategies affect significantly to the overall LCOE results, primarily due to the AEP differences. However, differences in the optimal platform de-

signs are minimal, suggesting that the couplings between control and plant might be negligible in the presented FloatVAWT configuration and modeling strategy. This partially suggests that sequential design might be potentially cost-effective design process if floating platform provides highly stable foundation for turbine structure. However, this finding must be limited to highly stable TLP cases and design strategy constraining thrust and side to side forces.

Overall, our study provides valuable insights into the modeling and optimization of FloatVAWT systems and highlights the potential for VAWTs to be a cost-effective solution for FOWTs. However, as our system-level modeling approach assumes various simplifications, further research is required to investigate the feasibility and practicality of implementing the proposed design in the later-stage design process.

REFERENCES

[1] Lopez, Anthony, Green, Rebecca, Williams, Travis et al. "Offshore Wind Energy Technical Potential for the Contiguous United States." Technical Report No. NREL/PR-6A20-83650. National Renewable Energy Laboratory. 2022.

[2] Stehly, Tyler, Duffy, Patrick and Hernando, Daniel Mulas. "2022 Cost of Wind Energy Review." Technical Report No. NREL/PR-5000-88335. National Renewable Energy Laboratory. 2023. DOI 10.2172/2278805.

[3] "A Low-Cost Floating Offshore Vertical Axis Wind System." U. S. Department of Eneergy Advanced Research Projects Agency-Energy (2020). Accessed March 12, 2024, URL https://arpa-e.energy.gov/technologies/projects/low-cost-floating-offshore-vertical-axis-wind-system.

[4] Jonkman, Jason. "The New Modularization Framework for the FAST Wind Turbine CAE Tool." *AIAA Aerospace Sciences Meeting*. AIAA 2013-0202. Grapevine, TX, Jan 7–10, 2013. DOI 10.2514/6.2013-202.

[5] Marten, David. "QBlade: A Modern Tool for the Aeroelastic Simulation of Wind Turbines." Ph.D. Thesis, Technische Universität Berlin, Berlin, Germany. 2019. DOI 10.14279/depositonce-10646.

[6] Jonkman, Jason, Wright, Alan, Barter, Garrett, Hall, Matthew, Allison, James and Herber, Daniel R. "Functional Requirements for the WEIS Toolset to Enable Controls Co-Design of Floating Offshore Wind Turbines." *ASME International Offshore Wind Technical Conference*. IOWTC2021-3533: p. V001T01A007. Virtual, Online, Feb 16–17, 2021. DOI 10.1115/IOWTC2021-3533.

[7] Lemmer, Frank, Yu, Wei, Luhmann, Birger, Schlipf, David and Cheng, Po Wen. "Multibody Modeling for Concept-Level Floating Offshore Wind Turbine Design." *Multi-*

body System Dynamics Vol. 49 (2020): pp. 203–236. DOI 10.1007/s11044-020-09729-x.

[8] Al-Solihat, Mohammed Khair and Nahon, Meyer. "Flexible Multibody Dynamic Modeling of a Floating Wind Turbine." *International Journal of Mechanical Sciences* Vol. 142–143 (2018): pp. 518–529. DOI 10.1016/j.ijmecsci.2018.05.018.

[9] Sundarrajan, Athul K., Lee, Yong Hoon, Allison, James T., Zalkind, Daniel S. and Herber, Daniel R. "Open-Loop Control Co-Design of Semisubmersible Floating Offshore Wind Turbines Using Linear Parameter-Varying Models." *Journal of Mechanical Design* Vol. 146 No. 4 (2024): p. 041704. DOI 10.1115/1.4063969.

[10] Lee, Yong Hoon, Bayat, Saeid and Allison, James T. "Control Co-Design Using a Nonlinear Wind Turbine Dynamic Model Based on OpenFAST Linearization." *Applied Energy Symposium: MIT A+B*. Cambridge, MA, Jul 5–8, 2022.

[11] Bayat, Saeid, Lee, Yong Hoon and Allison, James T. "Nested Control Co-design of a Spar Buoy Horizontal-axis Floating Offshore Wind Turbine." *ArXiv e-prints* (2023). URL https://arxiv.org/abs/2310.15463.

[12] Gao, Ju, Griffith, D. Todd, Sakib, Mohammad Sadman and Boo, Sung Youn. "A Semi-Coupled Aero-Servo-Hydro Numerical Model for Floating Vertical Axis Wind Turbines Operating on TLPs." *Renewable Energy* Vol. 181 (2022): pp. 692–713. DOI 10.1016/j.renene.2021.09.076.

[13] Fowler, Matthew J., Owens, Brian, Bull, Diana, Goupee, Andrew J., Hurtado, John, Griffith, D. Todd and Alves, Marco. "Hydrodynamic Module Coupling in the Offshore Wind Energy Simulation (OWENS) Toolkit." *International Conference on Offshore Mechanics and Arctic Engineering*. OMAE2014-24175: p. V09BT09A027. San Francisco, CA, Jun 8–13, 2014. DOI 10.1115/OMAE2014-24175.

[14] Lao, Yejun, Rotea, Mario A., Koeln, Justin P., Sakib, Mohammad S. and Griffith, Daniel Todd. "Nonlinear Model Predictive Control of Floating Offshore Vertical-Axis Wind Turbines." *Renewable Energy* pp. 1–29. DOI 10.2139/ssrn.4167679. Preprint.

[15] Le Fouest, Sébastien and Mulleners, Karen. "Optimal Blade Pitch Control For Enhanced Vertical-Axis Wind Turbine Performance." *Nature Communications* Vol. 15 No. 2770 (2024): pp. 1–13. DOI 10.1038/s41467-024-46988-0.

[16] Bouzaher, Mohamed Taher and Hadid, Mohamed. "Active Control of the Vertical Axis Wind Turbine by the Association of Flapping Wings to Their Blades." *Procedia Computer Science* Vol. 52 (2015): pp. 714–722. DOI 10.1016/j.procs.2015.05.083.

[17] Ahsan, Faraz, Griffith, D. Todd and Gao, Ju. "Modal Dynamics And Flutter Analysis Of Floating Offshore Vertical Axis Wind Turbines." *Renewable Energy* Vol. 185 (2022): pp. 1284–1300. DOI 10.1016/j.renene.2021.12.041.

[18] Gao, Ju, Griffith, D. Todd, Jafari, Mohammad, Yao, Shulong and Ahsan, Faraz. "Impact of Rotor Solidity on the Design Optimization of Floating Vertical Axis Wind Turbines." *International Conference on Offshore Mechanics and Arctic Engineering*. OMAE2022-78715: p. V008T09A019. Hamburg, Germany, June 5–10, 2022. DOI 10.1115/OMAE2022-78715.

[19] Buchner, Abel-John, Soria, Julio, Honnery, Damon and Smits, Alexander J. "Dynamic Stall in Vertical Axis Wind Turbines: Scaling and Topological Considerations." *Journal of Fluid Mechanics* Vol. 841 (2018): pp. 746–766. DOI 10.1017/jfm.2018.112.

[20] Tjiu, Willy, Marnoto, Tjukup, Mat, Sohif, Ruslan, Mohd Hafidz and Sopian, Kamaruzzaman. "Darrieus Vertical Axis Wind Turbine for Power Generation II: Challenges in HAWT and the Opportunity of Multi-Megawatt Darrieus VAWT Development." *Renewable Energy* Vol. 75 (2015): pp. 560–571. DOI 10.1016/j.renene.2014.10.039.

[21] Lee, Yong Hoon, Boo, Sung Youn and Allison, James T. "A Framework for Integrating Hydrostatics, Hydrodynamics, and Rigid-Body Dynamics for the Control Co-Design of Floating Offshore Vertical-Axis Wind Turbine Systems." *Wind Energy Science Conference*. 1345. Hannover, Germany, May 25–28, 2021.

[22] Sakib, Mohammad Sadman, Griffith, D. Todd, Hossain, Sanower, Bayat, Saeid and Allison, James T. "Intracycle RPM Control for Vertical Axis Wind Turbines." *Wind Energy* Vol. 27 No. 3 (2024): pp. 202–224. DOI 10.1002/we.2885.

[23] Lambe, Andrew B. and Martins, Joaquim R. R. A. "Extensions to the Design Structure Matrix for the Description of Multidisciplinary Design, Analysis, and Optimization Processes." *Structural and Multidisciplinary Optimization* Vol. 46 No. 2 (2012): pp. 273–284. DOI 10.1007/s00158-012-0763-y.

[24] Powell, Mike J. D. "A Direct Search Optimization Method That Models the Objective and Constraint Functions by Linear Interpolation." Gomez, S. and Hennart, J. P. (eds.). *Advances in Optimization and Numerical Analysis*. Springer, Dordrecht (1994): pp. 51–67. DOI 10.1007/978-94-015-8330-5_4.

[25] Newman, J. N. "Wave Effects on Deformable Bodies." *Applied Ocean Research* Vol. 16 No. 1 (1994): pp. 47–59. DOI 10.1016/0141-1187(94)90013-2.

[26] Al-Solihat, Mohammed Khair and Nahon, Meyer. "Stiffness of Slack and Taut Moorings." *Ships and Offshore Structures* Vol. 11 No. 8 (2016): pp. 890–904. DOI 10.1080/17445302.2015.1089052.

[27] "Wind Energy Generation Systems - Part 3-2: Design Requirements for Floating Offshore Wind Turbines." Technical Report No. IEC TS 61400-3-2. International Electrotechnical Commission. 2019. URL https://webstore.iec.ch/publication/29244.

[28] Murray, Jonathan and Barone, Matthew. "The Development of CACTUS, a Wind and Marine Turbine Performance Simulation Code." *AIAA Aerospace Sciences Meeting*. AIAA 2011-147: pp. 1–21. Reston, VA, Jan 4–7, 2011. DOI 10.2514/6.2011-147.

[29] Garg, Divya, Patterson, Michael A., Francolin, Camila, Darby, Christopher L., Huntington, Geoffrey T., Hager, William W. and Rao, Anil V. "Direct Trajectory Optimization and Costate Estimation of Finite-Horizon and Infinite-Horizon Optimal Control Problems Using a Radau Pseudospectral Method." *Computational Optimization and*

Applications Vol. 49 No. 2 (2011): pp. 335–358. DOI 10.1007/s10589-009-9291-0.

[30] Falck, Robert, Gray, Justin S., Ponnapalli, Kaushik and Wright, Ted. "Dymos: A Python Package for Optimal Control of Multidisciplinary Systems." *Journal of Open Source Software* Vol. 6 No. 59 (2021): p. 2809. DOI 10.21105/joss.02809.

APPENDIX A. GEOMETRY, MASSES, VERTICAL CENTERS OF GRAIVITY, AND MOMENTS OF INERTIA

The submerged portion of the TLP components' cross-sectional areas, volumes, and masses are given as:

$$A_{\text{sm},\#c} = \frac{\pi D_{\text{sm},\#c}^2}{4}, \tag{8a}$$

$$A_{\text{pont}} = \left(L_{\text{pont}} - \frac{D_{\text{cc}} + D_{\text{oc}}}{2} \right) W_{\text{pont}}, \tag{8b}$$

$$V_{\text{sm}} = H_{\text{dr}} \left(A_{\text{sm,cc}} + 3 A_{\text{sm,oc}} \right) + 3 H_{\text{sm,pont}} A_{\text{sm,pont}}, \tag{8c}$$

$$m_{\text{sm},\#c} = \int_{-H_{\text{dr}}}^{0} \mathbb{R}_{\text{sm},\#c} \left(A_{\#c}, h \right) \, dh, \tag{8d}$$

$$m_{\text{pont}} = \int_{-H_{\text{dr}}}^{-H_{\text{dr}}+H_{\text{pont}}} \mathbb{R}_{\text{pont}} \left(A_{\text{pont}}, h \right) \, dh, \tag{8e}$$

where D, W, H, L, A, V, m represent diameter, width, height, length, area, volume, and mass, respectively. Subscript sm denotes submerged portion, cc denotes center column, oc denotes outer column, #c denotes any column (either cc or oc), pont denotes pontoon, and dr denotes draught. Functions $\mathbb{R}$ are the empirical mass density regression function. They are created based on a proprietary TLP design database. The buoyancy force created by the submerged portion of the TLP is given as:

$$F_{\text{buoy}} = \rho_{\text{water}} V_{\text{sm}} g, \tag{9}$$

where ρ_{water} is ocean water density at sea surface and g is gravitational acceleration at ocean surface level. The freeboard (above water level) portion of the quantities are given as:

$$A_{\text{fb},\#c} = \frac{\pi D_{\text{fb},\#c}^2}{4}, \tag{10a}$$

$$V_{\text{fb}} = (H_{\text{cc}} - H_{\text{dr}}) A_{\text{fb,cc}} + 3 (H_{\text{oc}} - H_{\text{dr}}) A_{\text{fb,oc}}, \tag{10b}$$

$$m_{\text{fb},\#c} = (H_{\#c} - H_{\text{dr}}) \mathbb{R}_{\text{fb},\#c} \left(A_{\#c} \right), \tag{10c}$$

where subscript fb denotes freeboard. The regression function used for the freeboard portion does not vary over vertical location, so the function only takes the cross-sectional area as the parameter. The overall TLP mass and in-place system mass are:

$$m_{\text{ptfm}} = m_{\text{sm,cc}} + m_{\text{fb,cc}} + 3 \left(m_{\text{sm,oc}} + m_{\text{fb,oc}} + m_{\text{pont}} \right) \tag{11a}$$

$$m_{\text{sys}} = m_{\text{ptfm}} + m_{\text{turb}} + m_{\text{bal}}, \tag{11b}$$

where subscript ptfm denotes floating platform, sys denotes system at in-place condition, turb denotes turbine system (tower, rotor, and generator), and bal denotes ballast water.

Vertical COGs (VCGs) are calculated as:

$$\text{VCG}_{\text{sm},\#c} = \frac{1}{m_{\text{sm},\#c}} \int_{-H_{\text{dr}}}^{0} h \cdot \mathbb{R}_{\text{sm},\#c} \left(A_{\#c}, h \right) \, dh, \tag{12a}$$

$$\text{VCG}_{\text{fb},\#c} = \frac{1}{m_{\text{fb},\#c}} \frac{(H_{\#c} - H_{\text{dr}})^2}{2} \mathbb{R}_{\text{fb},\#c} \left(A_{\#c} \right), \tag{12b}$$

$$\text{VCG}_{\text{pont}} = \frac{1}{m_{\text{pont}}} \int_{-H_{\text{dr}}}^{-H_{\text{dr}}+H_{\text{pont}}} h \cdot \mathbb{R}_{\text{pont}} \left(A_{\text{pont}}, h \right) \, dh, \tag{12c}$$

$$\text{VCG}_{\text{sys}} = \frac{\left[\begin{array}{l} m_{\text{sm,cc}} \text{VCG}_{\text{sm,cc}} + m_{\text{fb,cc}} \text{VCG}_{\text{fb,cc}} \\ + 3 \left(m_{\text{sm,oc}} \text{VCG}_{\text{sm,oc}} + m_{\text{fb,oc}} \text{VCG}_{\text{fb,oc}} \right. \\ \left. + m_{\text{pont}} \text{VCG}_{\text{pont}} \right) + m_{\text{turb}} \text{VCG}_{\text{turb}} \end{array} \right]}{m_{\text{sys}}}. \tag{12d}$$

The system MOIs with respect to the system COG for roll (xx), pitch (yy), and yaw (zz) DOFs are calculated based on MOIs and radii of gyration of all the components of TLP, given as:

$$I_{xx,\text{sys}} = m_{\text{sys}} R_{xx,\text{sys}}^2, \tag{13a}$$

$$I_{yy,\text{sys}} = m_{\text{sys}} R_{yy,\text{sys}}^2, \tag{13b}$$

$$I_{zz,\text{sys}} = m_{\text{sys}} R_{zz,\text{sys}}^2. \tag{13c}$$

Here, radii of gyration (R) for these DOFs are calculated as:

$$R_{ii,\text{sys}} = \sqrt{\frac{\left[\begin{array}{l} I_{ii,\text{cc}} + I_{ii,\text{oc,fr}} + 2 I_{ii,\text{oc,si}} \\ + I_{ii,\text{pont,fr}} + 2 I_{ii,\text{pont,si}} + I_{ii,\text{turb}} \end{array} \right]}{m_{\text{sys}}}}, \quad ii = \left\{ \begin{array}{l} xx \\ yy \end{array} \right. \tag{14a}$$

$$R_{zz,\text{sys}} = \sqrt{\frac{I_{zz,\text{cc}} + 3 \left(I_{zz,\text{oc}} + I_{zz,\text{pont}} \right) + I_{zz,\text{turb}}}{m_{\text{sys}}}}, \tag{14b}$$

where subscript fr denotes front and si denotes side. Since the TLP has three outer columns with 60° apart from each other, their radii of gyration need to be translated in the Cartesian coordinates view. Front location refers to $-x$ direction, while side locations refer to $\pm y$ directions. MOIs for each TLP component are calculated by integrating the distance squared value multiplied by the mass density functions. Distances used for integration are calculated using the Euclidean distance between the system COG and the location of the integrand, and details are omitted for brevity.

Finally, the overall mass matrix of the system, M_{sys} is given as:

$$M = \begin{bmatrix} m & 0 & 0 & 0 & m\text{VCG} & 0 \\ 0 & m & 0 & -m\text{VCG} & 0 & 0 \\ 0 & 0 & m & 0 & 0 & 0 \\ 0 & -m\text{VCG} & 0 & I_{xx} & 0 & 0 \\ m\text{VCG} & 0 & 0 & 0 & I_{yy} & 0 \\ 0 & 0 & 0 & 0 & 0 & I_{zz} \end{bmatrix} \tag{15}$$

where subscript sys is omitted for brevity from all variables used in Eq. (15). The system COG is located at the exact center in $x - y$ directions. Thus, terms related to COG_y and COG_z in Eq. (15) could be kept zeros.